Spring 2010

Considerations for expanded very large array coronal Faraday Rotation measurements

Catherine Ann Whiting
University of Iowa

CONSIDERATIONS FOR EXPANDED VERY LARGE ARRAY CORONAL FARADAY ROTATION MEASUREMENTS

Catherine Ann Whiting

A thesis submitted in partial fulfillment of the
requirements for the Master of Science degree in Astronomy
in the Graduate College of The University of Iowa

May 2010

Thesis Supervisor: Professor Steven Spangler

Graduate College
The University of Iowa
Iowa City, Iowa

CERTIFICATE OF APPROVAL

MASTER'S THESIS

This is to certify that the Master's thesis of

Catherine Ann Whiting

has been approved by the Examining Committee
for the thesis requirement for the Master of
Science degree in Astronomy at the May 2010
graduation.

Thesis Committee: _____
Steven Spangler, Thesis Supervisor

_____
Robert Mutel

_____
Cornelia Lang

TABLE OF CONTENTS

LIST OF TABLES

Table

LIST OF FIGURES

Figure

CHAPTER 1
INTRODUCTION

1.1 Solar Corona

One of the remaining unexplained phenomena about our sun is the heating of its outer atmosphere, the corona. The surface temperature of the sun is approximately 6000 Kelvin, wheras farther out in the much less dense corona, the temperature can reach an unexpectely large value of one to a few million Kelvin, depending on whether coronal holes or closed field regions are present. A number of theories exist for why the solar corona has such a high temperature. Two main theories are wave heating through magneto-acoustic and Alfvén waves, which drive the solar wind, and the somewhat controversial theory of magnetic reconnection. Joule heating due to coronal current sheets is also a possible heating mechanism (Spangler 2007), as well as temperature inversion as a consequence of velocity filtration (Scudder 1992). Despite the apparent variety of explanations, it is evident that magnetic fields provide a common link among theories and play an important role in explaining coronal heating.

1.2 Faraday Rotation

Faraday Rotation is a phenomenon used as an observational technique in radio astronomy to study magnetic fields. The effect occurs with linearly polarized electromagnetic waves, which can be thought of as superpositions of right-hand and left-hand circularly polarized waves. The presence of a magnetic field in a medium results in a variable dielectric which depends on wave direction. As a linearly polarized wave passes through a medium with a magnetic field, the two circularly polarized waves propagate with different speeds. The resulting wave will then have a net rotation of its polarization position angle, $\Delta\chi$. The amount of rotation of the polarization position angle depends on the wavelength of the wave and the physical conditions of

the medium, defined by a quantity called the Rotation Measure (RM). The emergent polarization position angle, χ, is given by

$$\chi = \chi_o + RM\lambda^2 \tag{1.1}$$

where χ_o is the initial polarization position angle and λ is the wavelength of the observed radio wave. The net rotation of the polarization position angle is then given by

$$\Delta\chi = \lambda^2 \mathrm{RM} \tag{1.2}$$

where

$$\Delta\chi = \chi - \chi_o \tag{1.3}$$

Radio waves are ideal for Faraday rotation because the amount of rotation at radio wavelengths is measureable and a large number of linearly polarized radio sources exist. The RM (Ingleby et al. 2007) is given by

$$\mathrm{RM} = \frac{e^2}{2\pi m_e^2 c^4} \int_L n_e \vec{B} \cdot \vec{ds} \tag{1.4}$$

where e, m_e, and c are fundamental constants, the charge of an electron, the mass of an electron, and the speed of light, respectively, n_e is the plasma electron density, $\vec{B}$ is the vector magnetic field, and $\vec{ds}$ is the incremental path length along the line of sight. Equation 1.4 is given in cgs units, however, RM values are reported in SI units. The conversion from cgs to SI can be done by multiplying by a factor of 10^4. The observed quantity, $\Delta\chi$ is converted to a RM using Equation 1.2 and the desired physical quantity, the magnetic field[1] can be calculated from Equation 1.4. However, as Equation 1.4 shows, an independent estimate of the electron density is required. Fortunately, substantial information on the plasma density in the solar corona exists,

[1]It is important to note that only the line of sight component of the magnetic field can be recovered from Equation 1.4.

allowing for calculations of the magnetic field.

1.3 Past and Future Observations

1.3.1 Coronal Faraday Rotation

The Faraday rotation technique can be used to study magnetic fields in the solar corona. This is done by first observing a radio source when its line of sight is far from the sun, and measuring its linear polarization position angle, χ_o. The linear polarization position angle, χ, is then measured again when the line of sight to the source passes through the solar corona. The difference between these angles, $\Delta\chi$, is given by equation 1.3 and 1.2, from which the RM is obtained. Figure 1.1 illustrates this technique.

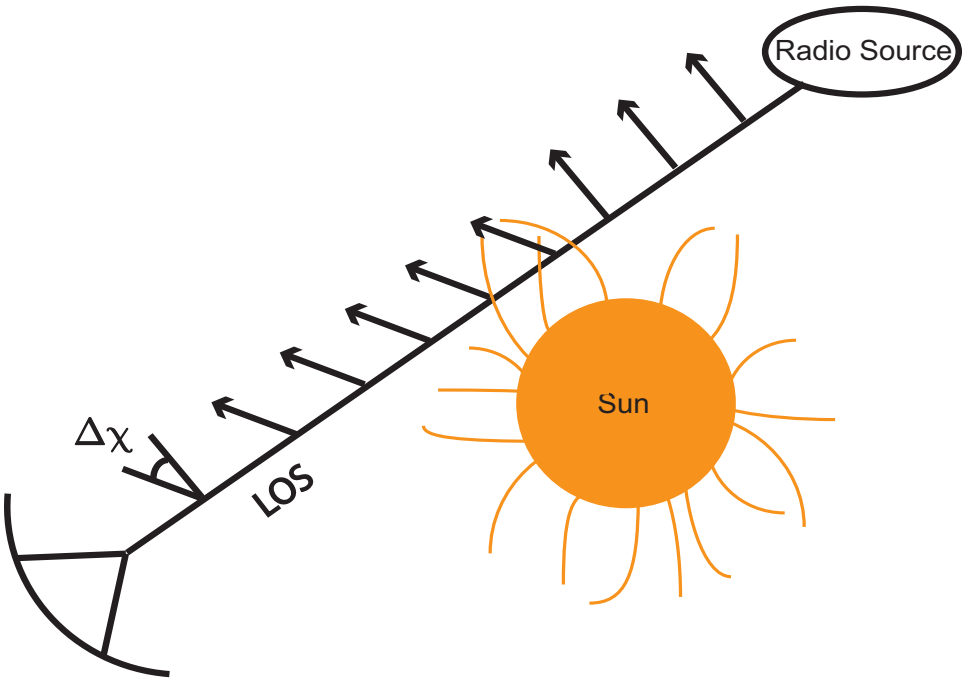

Figure 1.1: Illustration of Faraday Rotation technique. LOS is the line of sight.

One of the earliest uses of Faraday rotation in studying the line-of-sight component of the magnetic field in the solar corona was done in 1968 when the Pioneer

VI spacecraft was occulted by the sun (Stelzried et al. 1970). Its 2292 MHz signal underwent Faraday rotation and measurements of the magnetic field were obtained from 4 to 10 $R_\odot$ (1 $R_\odot$ is approximately $16'$). Faraday rotation measurements of the solar corona using an artificial radio source have also been attempted using the spacecraft HELIOS (Patzold et al. 1987). More recent studies have used natural linearly polarized radio sources, typically radio galaxies. One of the studies (Sakurai and Spangler 1994) observed 9 sources at 1465 and 1635 MHz, but the closest source had an angular separation of only 9 $R_\odot$ from the sun. Mancuso and Spangler (2000) observed 13 radio sources at 1465 and 1665 MHz, with the closest line of sight at 5 $R_\odot$. The most recent study (Ingleby et al. 2007) observed 20 radio sources, also at 1465 and 1665 MHz, with the closest source at 5.6 $R_\odot$. The studies of Sakurai and Spangler (1994), Mancuso and Spangler (2000), and Ingleby et al. (2007) were made with the Very Large Array (VLA) telescope. While all of these studies have been effective in measuring the plasma density and large-scale structure of the solar corona, the observations with the VLA were limited to a closest observing distance of about 5 $R_\odot$ from the sun. In order to fully understand the heating mechanisms of the solar corona, it is important to measure the magnetic field and plasma density between 2-5 $R_\odot$ as well, since it is probable that the heating mechanisms occur mostly in the inner, more dynamic corona.

1.3.2 Observational Challenges

The previous VLA studies were limited in their closest approach distance due to loss of sensitivity. The loss in sensitivity is due to increased rms noise in the image, which is proportional to the system temperature. The expected point source rms sensitivity due to thermal noise on a VLA image (Chandler 2009) is given by

$$\sigma_I = \frac{0.12 T_{sys}}{\eta_a \sqrt{N(N-1)(N_{IF}\tau\Delta\nu)}} \tag{1.5}$$

where σ_I is given in mJy, η_a is the antenna efficiency, N is the number of antennas, N_{IF} is the number of IF's used, τ is the integration time in hours, and $\Delta\nu$ is the bandwidth of the observation in MHz. The error in the polarization position angle, σ_χ is given by

$$\sigma_\chi = \frac{\sigma_Q}{2L} \tag{1.6}$$

where L is the polarized intensity of the source and σ_Q is the rms noise in the Stokes Q map. It is assumed throughout this thesis that σ_Q can be replaced with σ_I, which is true if all of the noise in the map is radiometer noise. Good observations result from either low noise measurements, effectively meaning low system temperatures, or sources with large polarized intensities. For observing distances of 2-5 $R_\odot$ at frequencies of 1.465 and 1.665 GHz it is extremely difficult to find sources with enough polarized intensity to overcome the high system temperatures of about 2000-4000 K (Geller 2004).

1.3.3 Future EVLA Observations

The solution to the observational challenges experienced by the previous VLA studies is to move to a higher observing frequency of 5 GHz. The 5 GHz beam pattern is smaller in angular size than the 1.465 and 1.665 GHz beam patterns, so the antenna response due to the contribution of the sun in the sidelobes is less for 5 GHz. This results in lower system temperatures and thus, better sensitivity. The main drawback of observing at 5 GHz is that the polarized intensity of a source decreases with increasing frequency, so according to Equation 1.6 σ_χ will increase. However, it is still possible to find radio sources with sufficiently large polarized intensities at 5 GHz.

The goal of this study is to test the feasibility of such observations at 5 GHz. To do this, it is necessary to (1) examine the expected rotation measures for 5 GHz between 2-5 $R_\odot$ from the sun, (2) measure the system temperature of the EVLA

antennas as a function of angular distance from the sun at 5 GHz, and (3) using the results of this, an evaluation of tolerable system temperatures for typical sources can be examined by comparing an expected $\Delta\chi$ with its expected error, σ_χ, for each source.

CHAPTER 2

ANTICIPATED VALUES OF CORONAL RM AT HELIOCENTRIC DISTANCES OF 2-5 $R_\odot$

Simple analytic expressions for the electron density and magnetic field are employed to provide an estimate of the expected RMs in the 2-5 $R_\odot$ region. If the expected RMs are large enough in comparison to the expected error in the RM, calculated from the rms noise in the images, then Faraday Rotation observations in this close region to the sun will be feasible. Two models of the coronal plasma structure are used to find an estimate of the expected RM's as a function of the "proximate distance," defined as the heliocentric distance of the closest point along the line of sight. The first model assumes a simple radial dependence of the electron density and magnetic field and is entitled "Single Power Law" given in Equations 2.1 and 2.2 (Ingleby et al. 2007). The second model, entitled "Compound Power Law," Equations 2.3 and 2.4, also assumes a radial dependence of the density and magnetic field, but has another term added to account for the density at large distances from the sun (Mancuso and Spangler 2000). A radially expanding solar wind justifies the simplification of using only radially dependent terms. Any non-radial components would be expected to be small.

$$n_e(r) = N_{os}(\frac{r}{R_\odot})^{-\alpha} \tag{2.1}$$

$$\vec{B}(r) = B_{os}(\frac{r}{R_\odot})^{-\delta}\hat{e}_r \tag{2.2}$$

$$n_e(r) = N_{oc}[A(\frac{r}{R_\odot})^{-\alpha_1} + B(\frac{r}{R_\odot})^{-\alpha_2}] \tag{2.3}$$

$$\vec{B}(r) = B_{oc}[C(\frac{r}{R_\odot})^{-\delta_1} + D(\frac{r}{R_\odot})^{-\delta_2}]\hat{e}_r \tag{2.4}$$

Figure 2.1 shows an illustration of the magnetic field model. The presence of a neutral line is necessary for a non-zero RM in these models, which assume radial dependence of the magnetic field. Since the RM is only dependent on the line-of-sight component of the magnetic field, a lack of reversal of the magnetic field direction

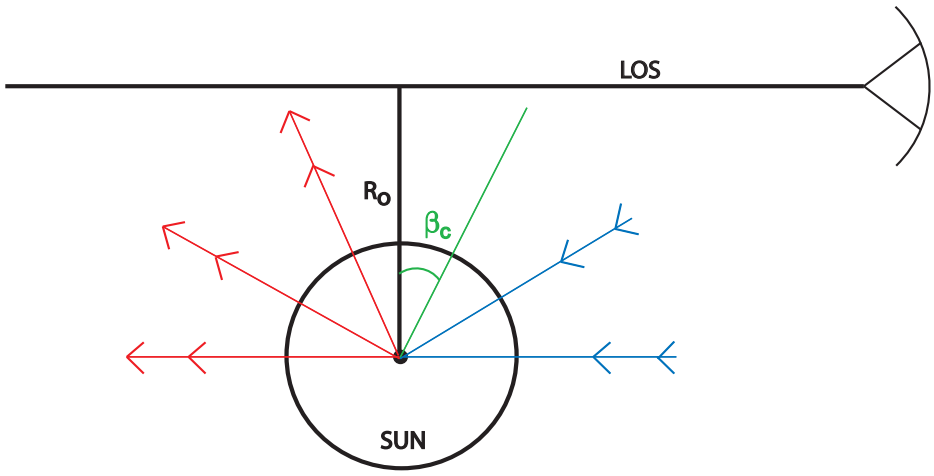

Figure 2.1: Illustration of coronal magnetic field model. Red lines represent outgoing magnetic field lines, blue lines represent ingoing magnetic fields lines, and the green line represents the neutral line where the polarity of the magnetic field reverses. β_c is defined as the angle between R_o and the neutral line. LOS is the line of sight.

would result in zero net RM. It is useful to introduce a heliocentric angle, β_c, which is measured between the neutral line and the point of closest approach of the line of sight to the center of the sun, defined to be R_o. Given Equations 2.1 and 2.2, and separately Equations 2.3 and 2.4, two new expressions (Equations 2.5 and 2.7)[2] for the RM can be derived (Spangler, private communication).

$$RM_{single}(R_o, \beta_c) = \frac{e^3 N_{os} R_\odot B_{os}}{\pi m_e^2 c^4 (\gamma - 1) R_o^{\gamma-1}} \cos^{\gamma-1}(\beta_c) \tag{2.5}$$

where

$$\gamma = \alpha + \delta \tag{2.6}$$

[2]Note that Equations 2.5 and 2.7 are only valid if there is one magnetic field reversal along the line of sight.

$$RM_{compound}(R_o, \beta_c) = \frac{e^3 N_{oc} R_\odot B_{oc}}{\pi m_e^2 c^4} \Big[\frac{AC}{(\gamma_1 - 1) R_o^{\gamma_1 - 1}} \cos^{\gamma_1 - 1}(\beta_c) + \frac{AD}{(\gamma_2 - 1) R_o^{\gamma_2 - 1}} \cos^{\gamma_2 - 1}(\beta_c) + \frac{BC}{(\gamma_3 - 1) R_o^{\gamma_3 - 1}} \cos^{\gamma_3 - 1(\beta_c)} + \frac{BD}{(\gamma_4 - 1) R_o^{\gamma_4 - 1}} \cos^{\gamma_4 - 1}(\beta_c) \Big] \tag{2.7}$$

where

$$\gamma_1 = \alpha_1 + \delta_1 \tag{2.8}$$

$$\gamma_2 = \alpha_1 + \delta_2 \tag{2.9}$$

$$\gamma_3 = \alpha_2 + \delta_1 \tag{2.10}$$

$$\gamma_4 = \alpha_2 + \delta_2 \tag{2.11}$$

The values used for the various parameters are given in Table 2.1. The Single Power Law values were given in Ingleby et al. (2007), and the Compound Power Law values were given by Spangler (private communication).

The results for both the single and compound power law RMs are shown in Figure 2.2. The value of β_c used in this calculation was chosen to be 0° to compare the maximum rotation measures of each model. Between 2 and 5 $R_\odot$ the rotation measures range from about 100-1000 rad/m^2 (which means $\Delta\chi$ is about 20-200° at 5 GHz) for the Single Power Law model. The Compound Power Law model estimates higher rotation measures, about 200-12000 rad/m^2 ($\Delta\chi$ is about 40-2500°) between 2 and 5 $R_\odot$. These results will be used in Chapter 5 to evaluate whether a typical source could be used for Faraday Rotation observations near the sun.

Table 2.1: Values of Model Parameters

Single	Value	Compound	Value
N_{os}	1.83 x 10^6cm^{-3}	N_{oc}	3.6 x 10^5cm^{-3}
B_{os}	1.01 G	B_{oc}	1.43 G
α	2.36	α_1	4.3
δ	2	δ_1	3
		α_2	2
		δ_2	2
γ	4.36	γ_1	7.3
		γ_2	6.3
		γ_3	5
		γ_4	4
		A	101
		B	1
		C	4.17
		D	1

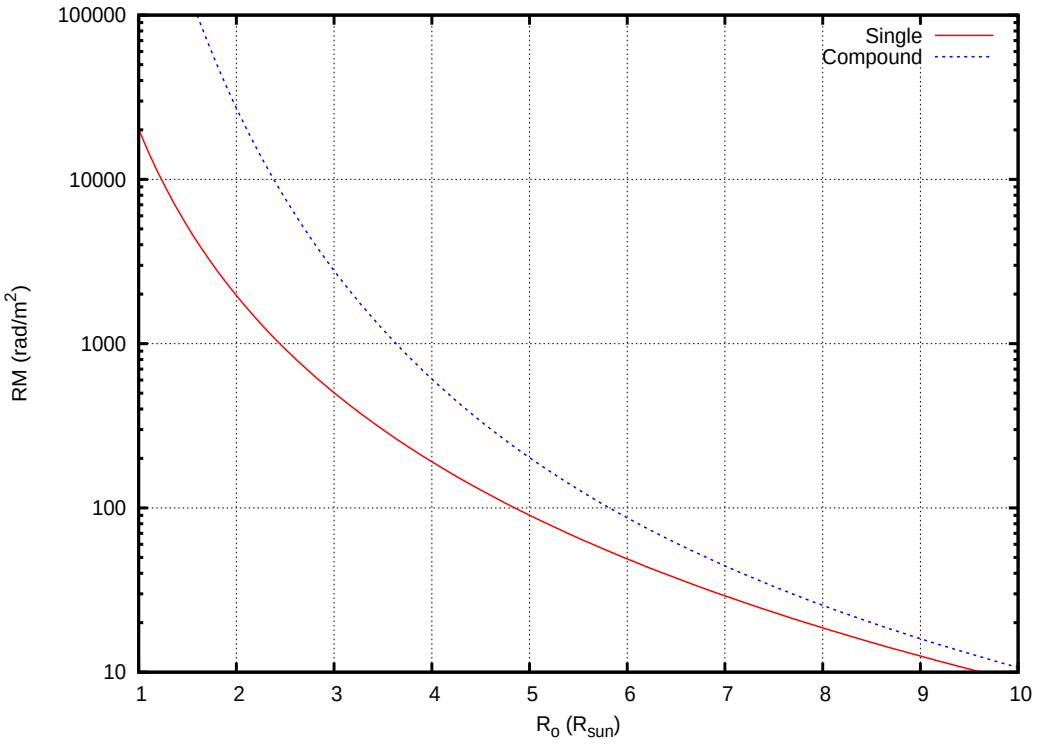

Figure 2.2: RM expectations for the Single and Compound Power Laws.

CHAPTER 3

SENSITIVITY OF THE EVLA AT 5 GHZ

EVLA Memo 136 [3]

3.1 Abstract

This document describes system temperature (T_{sys}) measurements near the sun at 5 GHz with EVLA antennas. The purpose of the test measurements was to measure the solar contribution to the system temperature as a function of angular distance from the sun. At a given angular separation from the sun, the antennas showed a range of system temperatures. The reason for this range is unclear. We based our results on the median T_{sys} of 10 antennas which provided adequate data. There are three significant regions of interest: at 2-3 $R_\odot$ (32-48′) the system temperature varies from 100-350 K; at 3-5 $R_\odot$ (48-80′) the system temperature is 50-100 K; for separations greater than 5 $R_\odot$ (80′) the system temperature levels off to the cold-sky EVLA T_{sys} value of 39 K. A model calculation of the system temperature due to the quiet sun in the sidelobes adequately reproduced the measured T_{sys} values.

3.2 Introduction

This document will describe test measurements made to determine the solar contribution to the system temperature as a function of solar offset. Observing near the sun can result in elevated system temperatures. Despite the loss in sensitivity due to this effect, there are many solar coronal phenomena that are interesting to measure. The motivation for these solar offset system temperature measurements is to plan for future solar coronal Faraday rotation observations. An example of such observations is described in Ingleby et al. (2007). The observations of Ingleby et al.

[3]Chapter 3 is a memo written by Catherine A. Whiting and Steven R. Spangler for the EVLA website: http://www.aoc.nrao.edu/evla/memolist.shtml. It appears here in its original form, with the exception of figure and equation numbers.

(2007) were made at 1.46 and 1.66 GHz and, due to system temperature constraints, were limited to a closest angular distance of 5 $R_\odot$ (80′). For our future observations we wish to observe closer to the sun, so we are switching to 5 GHz and are primarily interested in the performance of the EVLA from 2-5 $R_\odot$ (32-80′). The results of these test measurements may also be of interest to future observers making observations in the vicinity of the sun. This memo serves to provide that information.

The system temperature is the sum of the receiver temperature and the antenna temperature. The antenna temperature is determined by the antenna beam power pattern, which changes with observing frequency, and the angular separation of the beam center from the center of the sun. Since the antennas were not pointing directly at the sun throughout the observations, the side lobes were the main contribution to the system temperature. A theoretical model for the expected system temperature as a function of solar elongation will be discussed and describes the contribution of the sun in the side lobes.

3.3 Test Measurements

The observations were made on April 26, 2009 with 20 EVLA antennas. There were two IFs at 4885 MHz (IF 1) and 4835 MHz (IF 2) with right and left polarizations for each IF. Six antennas were edited out at the start due to lost data and an azimuth gearbox failure. The holography mode raster scan was chosen for the observing mode because of its ability to make measurements along a line segment with arbitrary starting point, length, and position angle with respect to the center of the sun. There were three scans starting at about 2 solar radii (32′) from the center of the sun. Throughout this document we will quote the solar offsets in units of both solar radii (which is relevant for planning coronal observations) and arcminutes. The solar radius value we used in quoting the offsets is the mean photospheric radius. The

conversion between solar radius and angular interval is

$$1R_{\odot} = 16' \ (arcminutes) \tag{3.1}$$

The actual photospheric radius on the day of observations was $15'.9$. The first scan was done at a position angle of 0°, labeled "Horizontal Scan". A position angle of 0° in the holography mode raster scan means to step in increasing azimuth with constant elevation. The second scan was at a position angle of 45°, labeled "Diagonal Scan", meaning equal steps in increasing elevation and azimuth at an angle of 45° with respect to the horizon, and the last scan was at a position angle of 90°, labeled "Vertical Scan", meaning steps in increasing elevation with azimuth constant. The elevation angle of the observations ranged from 63.5° - 69.3°. The antenna beam shape is not azimuthally symmetric (Perley and Hayward 2005) due to the quadrupod legs, so we chose the three different scans to check for possible effects of this on the system temperature. Each pointing was spaced by 0.18 $R_{\odot}$ ($2.9'$) and there were 38 pointings per scan, ending at 8.9 $R_{\odot}$ ($142'$). The horizontal scan was shortened (perhaps due to increased slew time of the antennas), and only had 26 pointings, extending out to 6.6 $R_{\odot}$ ($106'$).

The data were returned in the form of T_{sys} vs time in each of the two polarizations and two IFs. The desired observational function was $T_{sys}(r)$, where r is the angular offset from the sun, given in either solar radii or arcminutes. To obtain the antenna position in relation to the sun, we used the observe file and the time of each pointing and calculated the commanded position of the antennas. We do not have confirmation that the antennas were pointing at the commanded positions for the following reason. In the holography mode that we used it is necessary to have a reference antenna pointing at the center of the sun throughout the observations. This is because the holography mode only recognizes fixed antenna - moving antenna pairs and ignores pairs in which both antennas were moving. This is specific to the holography mode and we did not anticipate the need for this, so we did not use a

reference antenna during the observations. We have no reason to believe that the commanded positions were in error. Section 3.4.2. discusses a model which matches the data, indicating that our conversion of the antenna positions is correct.

3.4 Results

3.4.1 Measured Results

The system temperature data were retrieved with AIPS, using the PRTAB task accessing the system temperature extension file, TY. The values labeled "Tant" were interpreted as being the raw system temperature values. Figure 3.1 shows the raw system temperature data from the 14 EVLA antennas with useable data for the Vertical Scan, IF 1, polarization R. The plots for the other polarization-IF combinations were similar, as well as the data from the other two scans. The horizontal scan had a few low system temperatures at the beginning of the scan, possibly indicating a compression of the system temperature values for these measurements very close to the sun, or that the antennas had not yet reached their first position at 2 $R_\odot$ ($32'$) from the sun. In the next pointing of the Horizontal Scan, and the first 3 pointings of the Diagonal and Vertical Scans, a few of the antennas had relatively high system temperatures, some between 1000-3500 K. The main features of the raw T_{sys} measurements are that from 2-3 $R_\odot$ (32-$48'$) the system temperature ranges from about 100-350 K, from 3-5 $R_\odot$ (48-$80'$) the T_{sys} ranges from about 50-100 K, and from 5-8.9 $R_\odot$ (80-$142'$) the T_{sys} levels off to about 40 K. The constant system temperature past 8 $R_\odot$ ($128'$) seems to indicate that at this distance there is no solar contribution to the system temperature.

Near 9 $R_\odot$ ($143'$) the raw system temperatures for the various antennas range from about 20-50 K. This is interpreted as errors in the calibration of the system temperature, attributable to inaccurate values of the noise diode. This is of no consequence for normal interferometric observations, since most observers' calibration

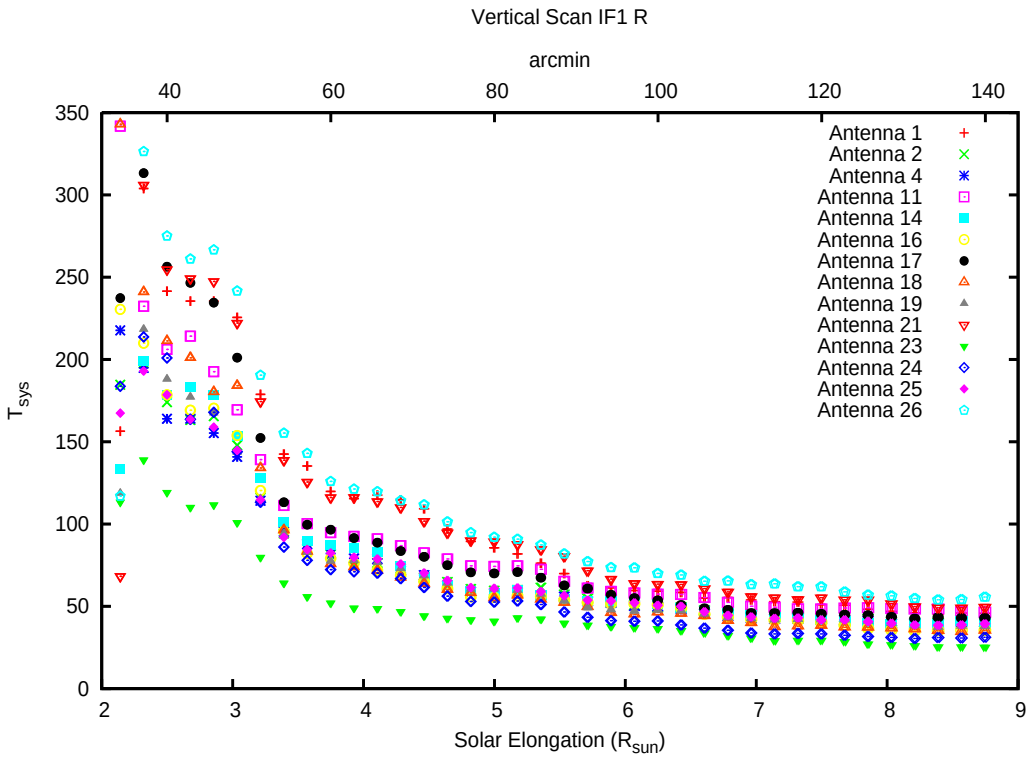

Figure 3.1: Unmodified system temperature data for 14 EVLA antennas

procedures absorb the errors into calibration constants. To average over this calibration error, we normalized the system temperatures to the median values at 8.9 $R_\odot$ (142′), and calculated a normalized temperature $T'(r)$ for each antenna, IF, and polarization, given by

$$T'(r) = T(r)\left[\frac{T_{median}}{T(r = 8.9R_\odot)}\right] \tag{3.2}$$

where $T(r)$ is the raw system temperature, $T(r = 8.9R_\odot)$ is the raw system temperature at the greatest angular separation for that antenna, polarization, and IF, and T_{median} is the median value of $T(r = 8.9R_\odot)$ for all 14 antennas with the same IF and polarization. The ratio $\left[\frac{T_{median}}{T(r = 8.9R_\odot)}\right]$ serves as a multiplicative normalization constant for each antenna, IF, and polarization. The normalized system temperatures as a function of r are shown in Figure 3.2. Figure 3.2 shows that, after normalizing the data, there was still significant spread in the system temperature values between antennas. At 2 $R_\odot$ (32′) the normalized system temperatures range from 100-350 K.

The reason for these inter-antenna differences is not entirely clear. Four antennas were eliminated from the data set at this point because they were at wide variance with the remaining antennas.

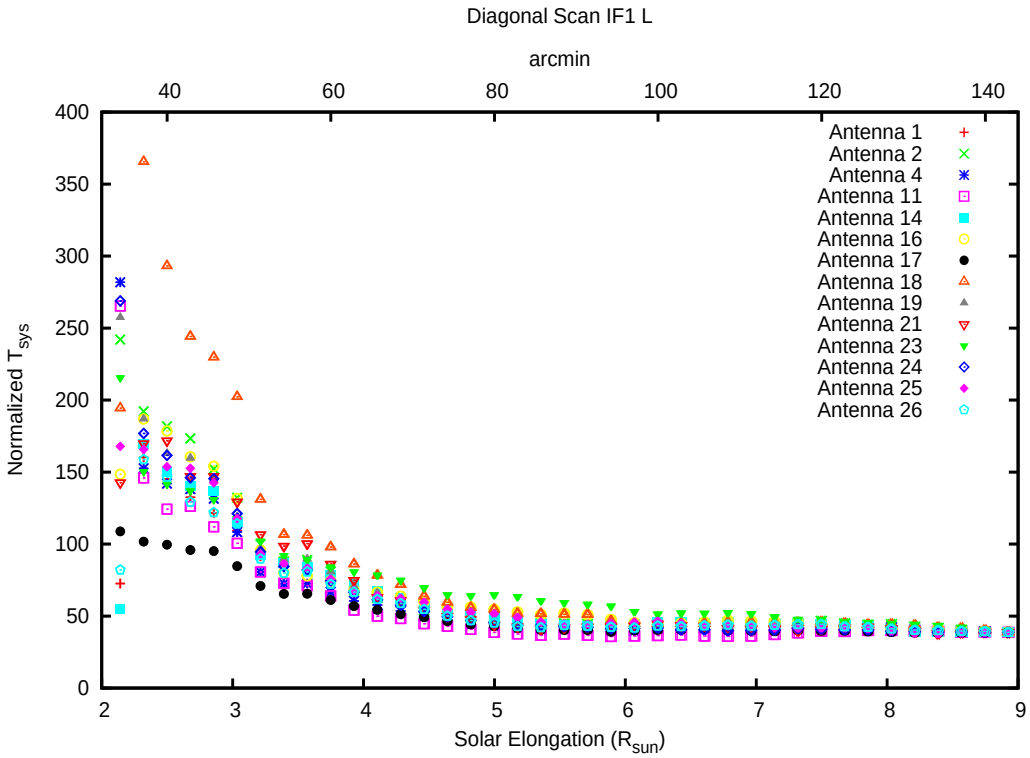

Figure 3.2: Normalized system temperature data calculated from Equation 3.2

We wished to condense the data shown in Figure 3.2 by taking a median of the normalized T_{sys} data. For most of the scans, a few of the antennas had significantly higher system temperatures than the others, as mentioned above, so we found it better to take a median of the data as opposed to a mean, since a median is less affected by outlying points. For each IF at a given solar elongation, T_{sys} measurements for all 10 antennas and both polarizations were included in the distributions from which we calculated the median and range. Instead of the standard deviation as a measure of the range, we chose the upper and lower limits which contained 80% of the measurements at a given pointing. The final result of this process was six

empirical functions for $\bar{T}'(r)$, corresponding to the 2 IFs for each of the 3 scans, where $\bar{T}'(r)$ is the median of the $T'(r)$ values. As an example, in Figure 3.3 we show $\bar{T}'(r)$ corresponding to IF 2 on the diagonal scan.

3.4.2 Comparison with Model Curves

The system temperature is a sum of the receiver temperature and the antenna temperature. The receiver temperature should be constant, but the antenna temperature changes when observing near the sun. The expected antenna temperature is proportional to the convolution of the beam power pattern with the brightness temperature distribution of the source. To understand our measurements shown in Figure 3.3, we calculated an a-priori estimate of the sun-induced antenna temperature as a function of angular offset. To this we added a receiver temperature value of 39 K to obtain a model function T(r). We used a uniform brightness temperature distribution from a VLA 4.6 GHz image of the quiet sun (Stephen White, Univ. of Maryland, private communication), with a brightness temperature of 15000 K (Zirin et al. 1991). For the beam power pattern we used Figure 5 from Perley and Hayward (2005), which plots the normalized beam power pattern for several slices through the 4850 MHz beam pattern of EVLA antenna 13. The solar radius used in the model calculation was $16'.25$, which is defined as the radius above a brightness temperature of 10000 K at 4.6 GHz for April 26.

Figure 3.3 shows the model $T(r)$ values plotted with the measured $\bar{T}'(r)$ values. The curve reproduces the data at 2-2.5 $R_\odot$ (32-40$'$) and does a very good job of reproducing the system temperature increase near 2 $R_\odot$ (32$'$). However, it subsequently falls off too fast to the receiver temperature value. The reason for this is that the beam power pattern of Perley and Hayward (2005) was only measured out to about 3 $R_\odot$ (48$'$), including only the first and second side lobes. The model curve does not include contributions to the antenna temperature from the antenna response beyond

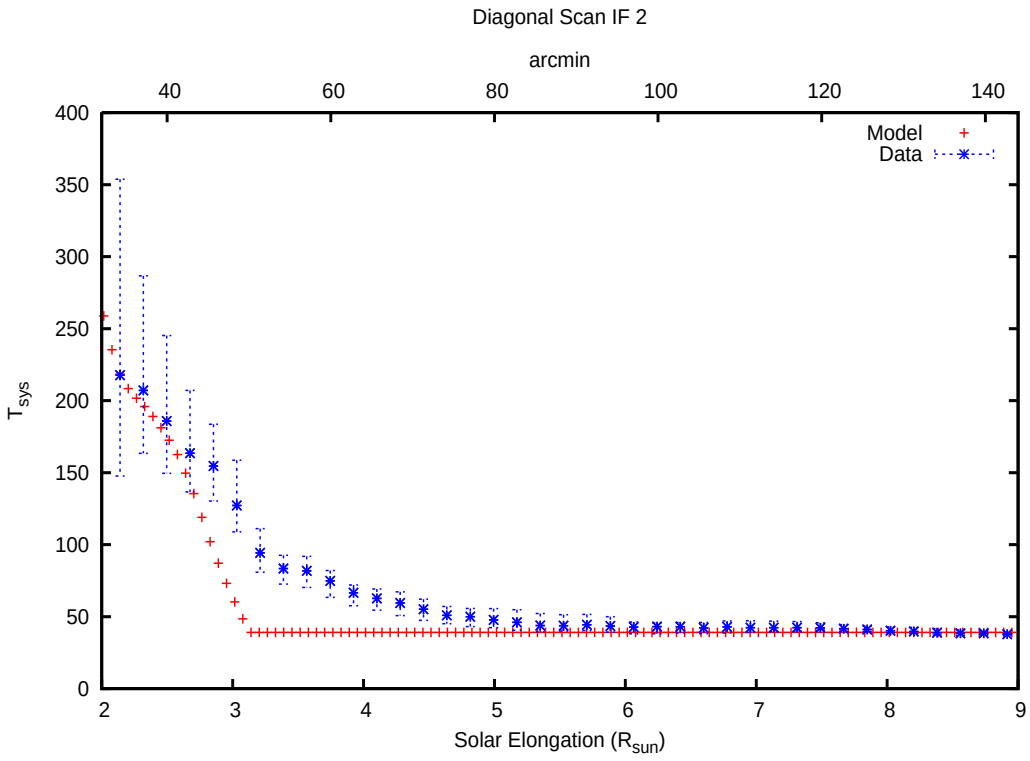

Figure 3.3: $\bar{T}'(r)$ for IF2 on the diagonal scan. The "error" bars represent the range which includes 80% of the antennas. The red crosses are system temperature expectations based on a model using the antenna beam pattern in Perley and Hayward (2005).

the second sidelobe. The obvious conclusion to be drawn from Figure 3.3 is that higher order sidelobes determine the solar contribution to the antenna temperature for r $\geq 3R_{\odot}$ ($48'$).

We estimated the role of additional sidelobes on the antenna temperature as follows. We created a plausible extrapolation of the beam power pattern based on the theoretical expression for a uniformly-illuminated circular aperture (Rohlfs and Wilson 2000),

$$P(r) = \left[\frac{2J_1(\pi r D/\lambda)}{\pi r D/\lambda}\right]^2 \tag{3.3}$$

where $J_1(x)$ is a Bessel Function of the first kind. We noticed that the first and

second[4] sidelobes of the measured power pattern were twice as high as predicted by Equation 3.3. Our estimate of the third sidelobe included this effect. We recalculated the model $T(r)$ with an extrapolated third sidelobe appended to the beam pattern of Perley and Hayward (2005). This third sidelobe had 0.3% of the forward gain (-25 dB) and peaked at 3.4 $R_\odot$ (55′) from the beam center. Calculation of a model $T(r)$ with a beam possessing the extrapolated and extended third sidelobe tended to overestimate the system temperature in comparison with the data. By a process of trial and error we determined a third sidelobe level which appeared to provide a good match to the measured data. The location of this third sidelobe was kept at the offset from the beam center indicated by Equation 3.3. A comparison of a model $T(r)$, including a third sidelobe level of 0.2% (-27 dB) of the forward gain is shown in Figure 3.4.

The addition of the extrapolated third sidelobe matches the data at separations greater than about 2.5 $R_\odot$ (40′). Between 2-2.5 $R_\odot$ (32-40′) the model slightly overestimates the median system temperature, yet it is well within the range of the data. Figure 3.4 indicates that a third sidelobe is needed in the model to reproduce the measured data. The underestimate of the system temperature in the model near 5 $R_\odot$ (80′) seems to indicate that side lobes of order higher than three may also be contributing to the system temperatures, although at a very low level.

Our main result is that the measured beam pattern, supplemented by a plausible though unmeasured third sidelobe, together with an independent representation of the brightness distribution of the quiet sun, provides a good representation of the measured 5 GHz system temperature of the EVLA. Figure 3.4 may be used in planning, and determining the sensitivity for, future EVLA observations at 5 GHz.

[4]After considering more realistic models for the power pattern, as discussed in the Appendix, it was discovered that the actual second sidelobe is suppressed due to the presence of the subreflector. What was referred to as the second sidelobe is actually the third sidelobe and what was referred to as the third sidelobe is actually the fifth sidelobe.

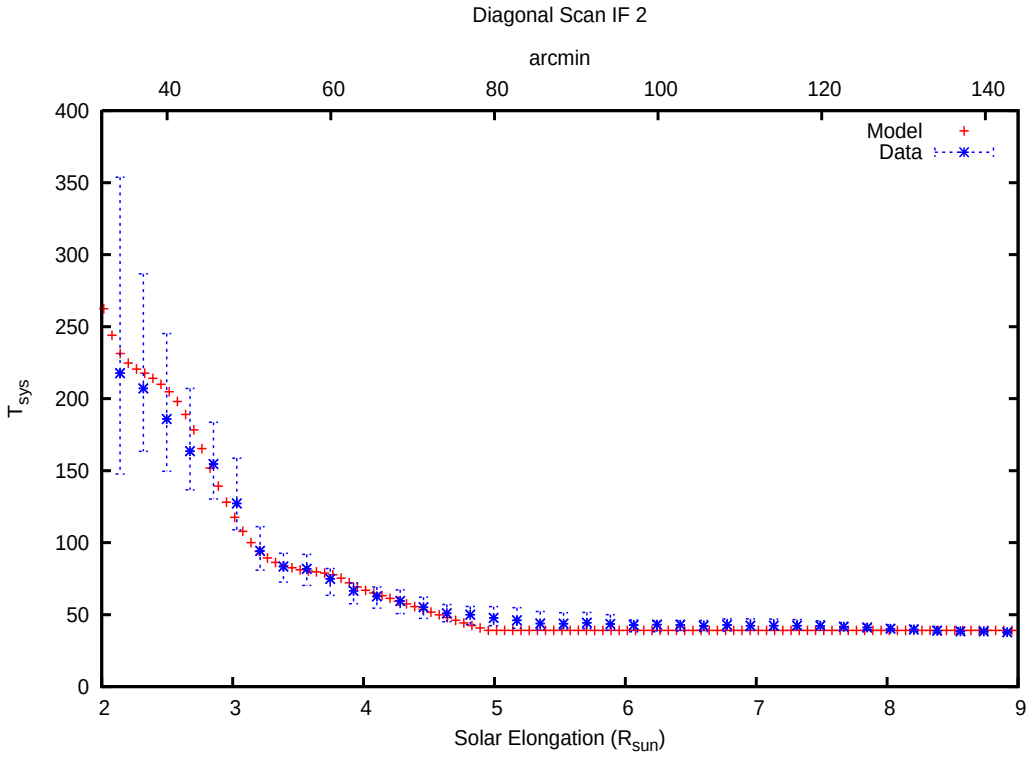

Figure 3.4: Red points represent the theoretical model using a plausible extrapolation of the antenna beam pattern past 3 $R_\odot$ (48′).

3.5 Summary

The results of this investigation are summarized below.

1. EVLA test measurements were taken on April 26, 2009 to measure the solar contribution to the system temperature at 5 GHz as a function of angular distance from the sun.

2. The EVLA antennas need calibration due to the observed spread of cold-sky system temperature values. Normally, this should not be a concern, since most calibration procedures account for this.

3. After normalization, the system temperatures still showed significant antenna-to-antenna variance, especially at 2-3 $R_\odot$ (32-48′). The reason for this is unknown.

4. The C-band system temperatures at a pointing offset of 8 solar radii (128′) and greater do not appear to show any T_{sys} enhancement due to the sun. From 3-5 $R_{\odot}$ (48-80′) the median system temperatures range from 50-100 K and between 2-3 $R_{\odot}$ (32-48′) they range from 100-350 K.

5. A theoretical model using an extrapolated antenna beam pattern can adequately represent the T_{sys} values as a function of solar offset.

6. A final point is that these measurements were made during the anomalously low solar minimum between solar cycles 23 and 24. It is probable that a future observer could experience higher system temperatures than those reported here, due to the presence of active regions on the sun.

CHAPTER 4

CALCULATION OF MODEL CURVE FOR $T(R)$

Chapter 3 describes model T_{sys} curves for comparison with the observed T_{sys} values ($\bar{T}'(r)$). This chapter provides a detailed description of the models and the way in which they were calculated.

The system temperature is a sum of the receiver temperature and the antenna temperature.

$$T_{sys} = T_A + T_R \tag{4.1}$$

The antenna temperature is of interest for the calculation because it is the component of the system temperature that is affected by the sun. It is proportional to the convolution of the antenna power pattern with the brightness temperature distribution of the source, where the origin of the coordinate system is chosen to be the center of the antenna power pattern.

$$T_A = \frac{\eta}{A} \int\int P_n(\theta, \phi) T_B(\theta, \phi) d\Omega \tag{4.2}$$

where η is the antenna efficiency, which is 60% for the ELVA at 5 GHz (Chandler 2009), $P_n(\theta, \phi)$ is the antenna beam power pattern, $T_B(\theta, \phi)$ is the brighteness temperature distribution of the source, and A is a normalization constant obtained by integrating $P_n(\theta, \phi)$ over 4π steradians.

Figure 4.1 is an illustration of how the calculation was performed. A simplification of Equation 4.2 using the illustration of Figure 4.1 results in the following equation for the antenna temperature.

$$T_A = \eta \frac{\int_{R_o - \Theta}^{R_o + \Theta} dr \int_{-\phi(r)}^{\phi(r)} d\theta r P(r, \theta) T_B(r, \theta)}{\int_0^{\infty} dr \int_0^{2\pi} d\theta P(r, \theta) r} \tag{4.3}$$

where Θ is the radius of the sun (above a brightness temperature of 10,000 K, or $16.25'$) and R_o is the distance from the line of sight (center of the beam pattern)

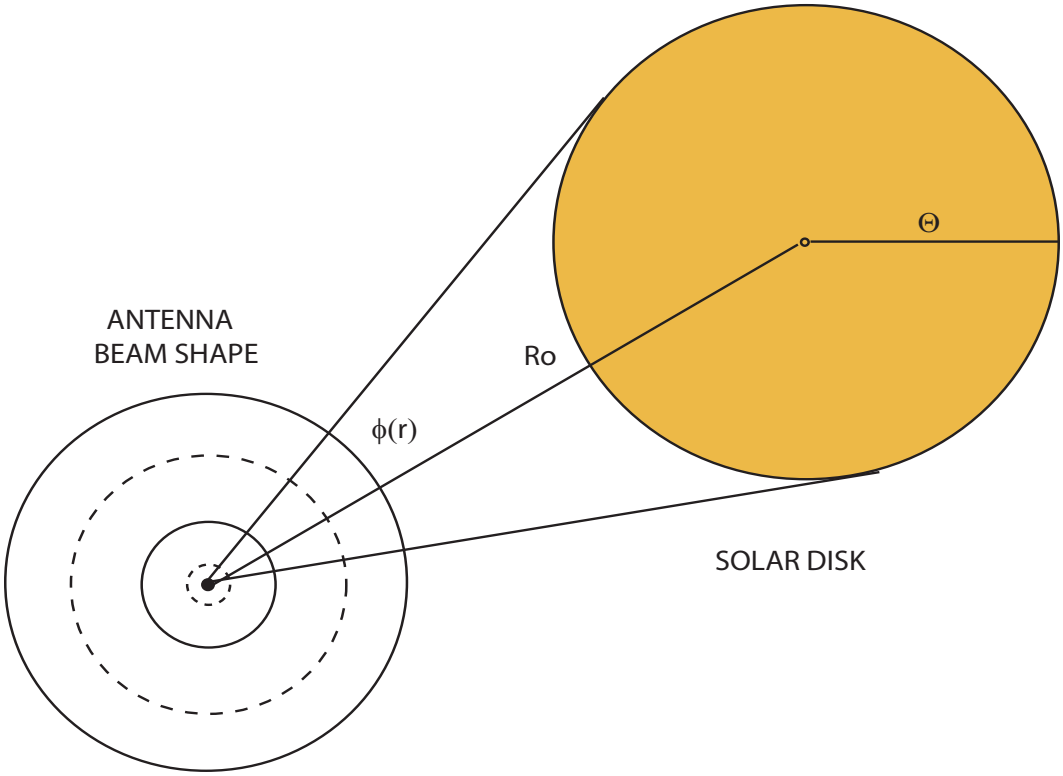

Figure 4.1: Illustration of simplified T_A calculation.

to the center of the sun. The origin of the coordinate system is chosen to be at the center of the beam pattern for convenience. ϕ is defined to be an angle which encloses the sun, and $\phi(r)$ is a function of the variable r, which has a value of zero at $R_o - \Theta$ and $R_o + \Theta$. Its form is given by

$$\phi(r) = \cos^{-1}\left(\frac{r^2 + R_o^2 + \Theta^2}{2R_o r}\right) \tag{4.4}$$

Equation 4.3 was solved using a summation approximation because the power pattern was given in a discrete, non-analytic form. The form of the 5 GHz power pattern for an EVLA antenna was given in Perley and Hayward (2005) and an extrapolation of this pattern was produced, as discussed in Chapter 3. The brightness temperature distribution of the sun was treated both as a uniform disk with a brightness temperature of 15,000 K and as a limb-darkened disk. The brightness distribution of the limb-darkened disk was based on a 5 GHz VLA image of the sun (courtesy of Stephen White, University of Maryland, private communication).

Model T_{sys}[5] values for the four scenarios are plotted in Figure 4.2. As expected, the models without the extended power pattern produce the smallest system temperatures, with the limb-darkened model producing the smallest. The models using the modified power pattern produce more realistic system temperatures, and the uniform brightness model is the best match to the data (see Chapter 3).

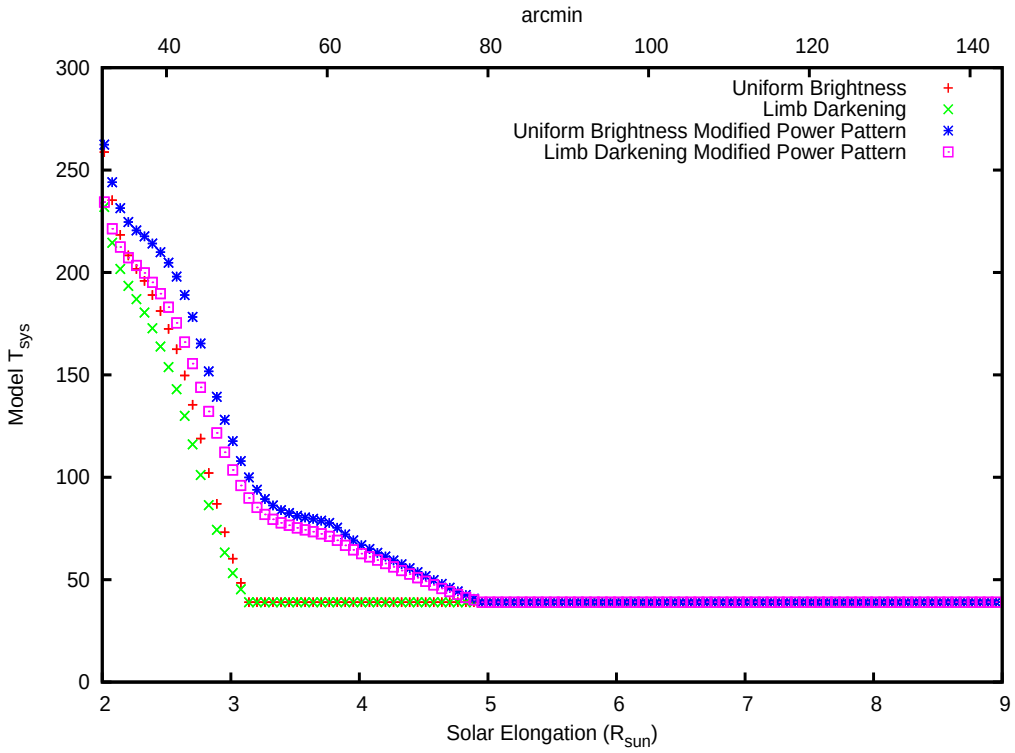

Figure 4.2: Model Tsys plotted against the photospheric radius of the sun (16 arcmin)

[5]The notation Model T_{sys} is equivalent to $T(r)$ in the EVLA Memo, Chapter 3.

CHAPTER 5

SENSITIVITY CALCULATIONS USING TYPICAL SOURCES

Suitable sources for coronal Faraday rotation observations are typically bright radio galaxies with a large amount of polarized intensity. Table 5.1 shows a sample of real sources found with the NRAO VLA Sky Survey[6] (Condon 1998) for which T_{sys}, σ_I, σ_χ, and $\Delta\chi$ have been calculated. The T_{sys} values are listed as the predicted values from the uniform brightness, modified power pattern model. Parameters for the calculation of σ_I were an integration time of 1 hour, a bandwidth of 50 MHz, one IF, and 25 antennas. The $\Delta\chi$ values were calculated using Equation 2.5 for the Single Power Law RM model.

It is evident that the predicted errors in the polarization position angle, σ_χ, are sufficiently small in comparison to the predicted polarization position angles, $\Delta\chi$, to allow for the proposed observations near the sun. An important note, however, is that the EVLA test observations were made during solar minimum (end of cycle 23, beginning of cycle 24) and the model T_{sys} values are from a uniform disk model. Future observations may encounter system temperatures that are elevated with respect to those presented here. Also, the calculated $\Delta\chi$ values were the maximum values predicted by the model ($\beta_c = 0$), so the difference between $\Delta\chi$ and σ_χ for a given source may not be as large as predicted.

[6]Polarized intensity values from the NRAO VLA Sky Survey survey were taken at 1.4 GHz. Conversion to polarized intensity values at 5 GHz was done with a spectral index value of -0.7.

Table 5.1: Typical Sources

Source	R_o ($R_\odot$)	L (mJy)	T_{sys} (K)	σ_I (mJy)	σ_χ (deg)	$\Delta\chi$ (deg)
4C +23.12	2.27	10.85	221	0.25	0.67	285
PKS 0520+23	2.83	4.81	152	0.18	1.0	133
MG2 J054400+2252	3.7	7.95	79	0.09	0.33	53.5
4C +23.11	4.14	4.34	63	0.07	0.48	36.7

CHAPTER 6

SUMMARY

The results of this thesis are summarized below.

1. Magnetic fields are crucial to understanding coronal heating. One of the most useful observational techniques for studying coronal magnetic fields is Faraday rotation.

2. Previous coronal Faraday rotation studies done at 1.4 and 1.6 GHz with the VLA were successful in obtaining an understanding of the large-scale structure of the plasma density and magnetic fields in the corona, but were limited to a closest angular approach of 5 $R_{\odot}$.

3. In future studies it is desirable to probe the inner, more dynamic corona up to 2 $R_{\odot}$, but to overcome the loss in sensitivity due to increased system temperatures, an observing frequency of 5 GHz must be used.

4. The purpose of this study was to determine whether such 5 GHz observations at 2-5 $R_{\odot}$ are feasible by doing the following:

   (a) Test observations with the EVLA were performed to determine the system temperature of each antenna as a function of angular offset from the sun.

   (b) A calculation of σ_{χ} for typical sources was calculated using predicted model T_{sys} values.

   (c) Two model calculations of the RM (converted to $\Delta\chi$) were performed to compare with the σ_{χ} values.

5. The results of the EVLA test observations are summarized in Section 3.5.

6. Model calculations of T_{sys} as a function of angular distance from the sun were

performed to confirm the observed T_{sys} values and be used as a tool for predicting T_{sys} values for various solar offsets.

7. The first RM model incorporates radially dependent, Single Power Law equations for $B(r)$ and $n_e(r)$ while the second model incorporates an additional radial term in each. The rotation measures in the region of 2-5 $R_\odot$ for the single power law equation range from 100 to 1000 rad/m^2, while the Compound Power Law equation yields values from about 200- 12,000 rad/m^2.

8. Sample calculations of T_{sys}, σ_χ and $\Delta\chi$ for real sources were performed to evaluate whether the σ_χ is significant in relation to the predicted $\Delta\chi$ values.

9. Given the results for σ_χ and $\Delta\chi$ in Table 5.1 it is evident that future solar coronal Faraday rotation observations with the EVLA at 5 GHz with solar offsets of 2-5 $R_\odot$ are feasible, provided that increased solar activity does not cause excessive increases in the system temperatures.

APPENDIX

During the defense of this thesis the question arose of whether a theoretical expression for the entire beam pattern, including an edge taper, could account for T_{sys} as a function of solar offset. To investigate this, new estimates of model T_{sys} values were calculated using three purely theoretical power patterns. The general expression for the normalized power pattern of a circular aperture is given by the square of the Hankel transform of the current grading, as shown in equation A.1 (Rohlfs and Wilson 2000).

$$P_n(u) = \left[\frac{\int_{\frac{d}{2\lambda}}^{\frac{D}{2\lambda}} g(r) J_0(2\pi u r) r dr}{\int_{\frac{d}{2\lambda}}^{\frac{D}{2\lambda}} g(r) r dr} \right]^2 \tag{A.1}$$

where $g(r)$ is the current grading, J_0 is the zeroth order Bessel function, D is the diameter of the EVLA primary reflector (25m), d is the diameter of the subreflector (2.35m) (Napier 1996), and λ is the observing wavelength. Three types of current gradings were used, one uniform and two tapered. One of the taper functions was given by equation A.2 with an edge taper of -12.5 dB, as mentioned in Srikanth et al. (2005). In order to produce the -12.5 dB edge taper the angle θ needed to be 86.8°. The other taper function (Christiansen and Högbom 1969), given by equation A.3, had an edge taper of -3 dB and the values of K and p were chosen to be 0.5 and 2, respectively.

$$g(r) = \cos\left(\frac{r}{\frac{D}{2\lambda}} \theta \right) \tag{A.2}$$

$$g(r) = K + \left[1 - \left(\frac{r}{\frac{D}{2\lambda}} \right)^2 \right]^p \tag{A.3}$$

Figure A.1 shows the normalized power patterns for each of the three types of current gradings. The addition of a "hole" in the illumination of the dish due to

the presence of the subreflector had a significant and interesting effect on the power patterns. The second, fourth, and sixth sidelobes are suppressed in all models, most significantly in the cosine taper model. The effect of the cosine taper seems to be to lower the sidelobe levels and to move them to larger offsets with respect to the uniform model. The first sidelobe in the taper model of Equation A.3 is also offset with respect to the uniform model, however, the positions of the rest of the sidelobes match those of the uniform model. The taper model of Equation A.3 is more affected by the presence of the subreflector than the uniform model.

The cosine taper model seems to be the best fit of the three to the measured power pattern given in Perley and Hayward (2005), in terms of the positions and widths of the first and third sidelobes. However, the sidelobe levels are significantly lower. The first sidelobe is about 3 to 8 dB lower than the measured pattern, depending on whether the cuts with the quadrupod legs are considered. The third sidelobe is significantly lower, about 10 dB lower than the measured pattern.

Figure A.2 shows the model T_{sys} results for the three power pattern models. The cosine taper model does not even produce system temperatures above 50 K for offsets greater than 2 $R_{\odot}$, while the taper model of Equation A.3 reaches only about 65 K near 2 $R_{\odot}$. The uniform model predicts the highest system temperatures, since the response of the higher order sidelobes is higher than in the tapered models, but it produces system temperatures less than 125 K for offsets greater than 2 $R_{\odot}$.

None of these analytic models match the data for offsets less than 5 $R_{\odot}$. The explanation for this is the low response of the sidelobes in the models. It is evident that the empirical extrapolation of the measured power pattern discussed in Chapter 3 is the best fit to the $\bar{T}'(r)$ data. In conclusion, these models do not match the observed system temperatures as a function of solar offset. The true antenna response at offsets greater than $40'$ is apparently larger than expected from these idealized theoretical models.

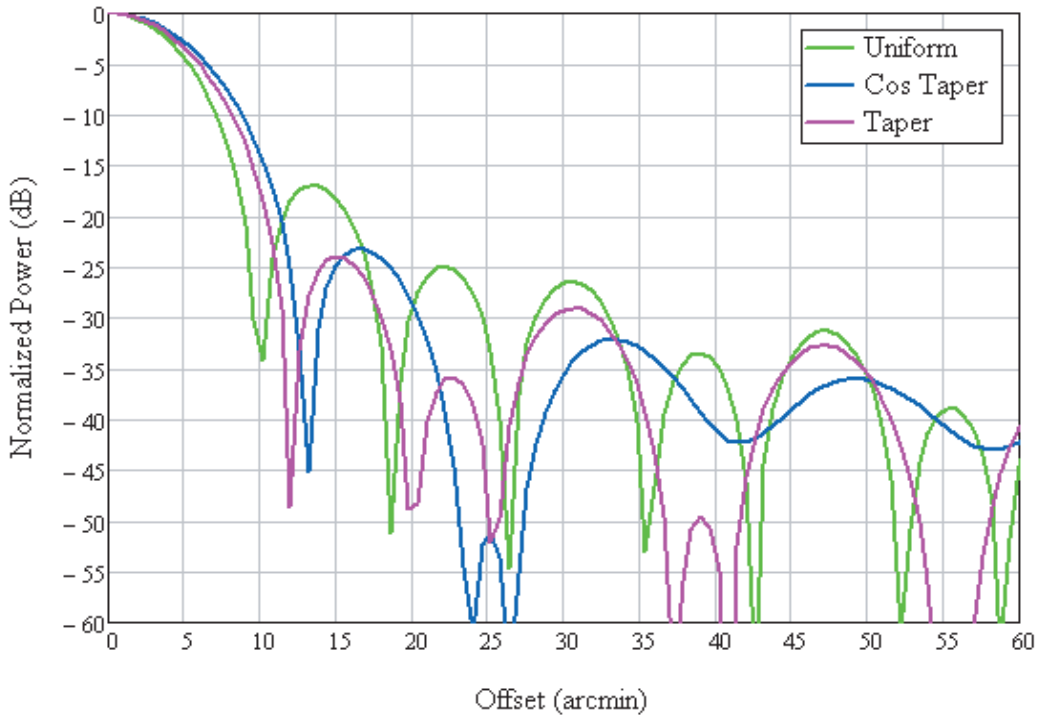

Figure A.1: Normalized power pattern models for three types of current gradings.

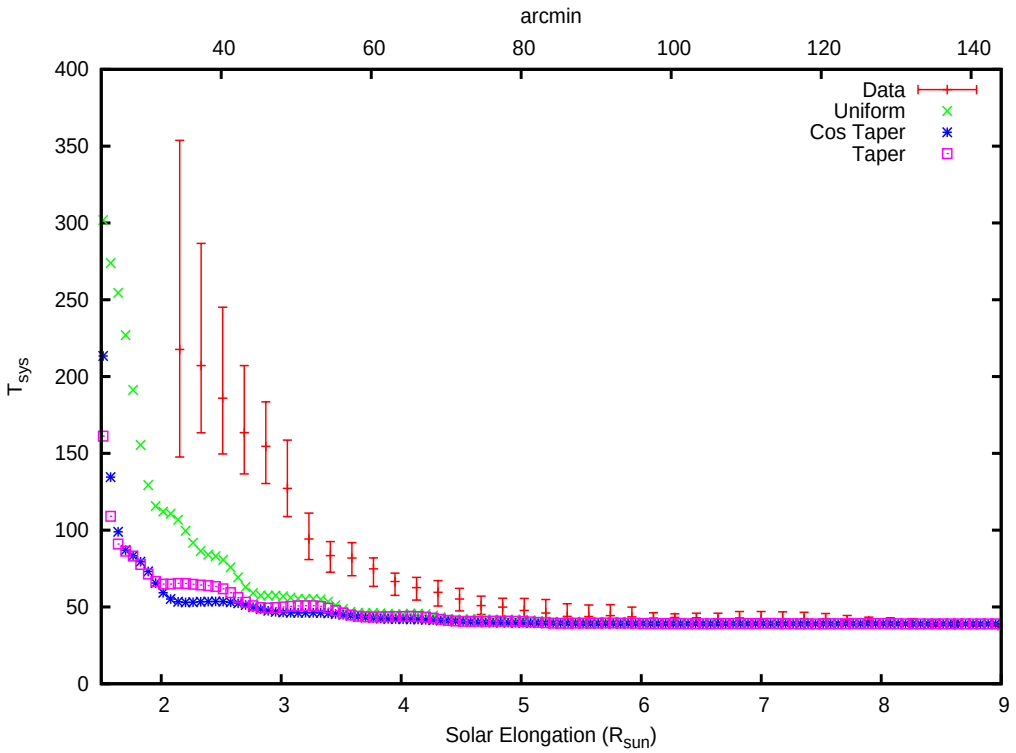

Figure A.2: Model T_{sys} values for three types of current gradings plotted against the EVLA data ($\bar{T}'(r)$).

REFERENCES

[1] C. Chandler, *Sensitivity*, http://www.vla.nrao.edu/astro/guides/vlas/current/node11.html#TAB:VLASENS, (2009).

[2] W.N. Christiansen and J.A. Högbom, *Radiotelescopes*, Cambridge University Press, (1969).

[3] J.J. Condon et al, *AJ* **115**, 1693 (1998).

[4] A. Geller, *The Sensitivity of a VLA Antenna During Near Sun Observations*, UI Undergraduate Honors Thesis, (2004).

[5] L.D. Ingleby, S.R. Spangler and C.A. Whiting, *ApJ* **370**, 779 (2007).

[6] S. Mancuso and S.R. Spangler, *ApJ* **539**, 480 (2000).

[7] P.J. Napier *EVLA Memo* **5**, (1996).

[8] M. Patzold, M.K. Bird, H. Volland, G.S. Levy, B.L. Seidel and C.T. Stelzried, *SoPh* **109**, 91 (1987).

[9] R. Perley and B. Hayward, *EVLA Memo* **90**, (2005).

[10] K. Rohlfs and T.L. Wilson, *Tools of Radio Astronomy*, Springer-Verlag, (2000).

[11] T. Sakurai and S.R. Spangler, *ApJ* **434**, 773 (1994).

[12] J.D. Scudder, *ApJ* **398**, 319 (1992).

[13] S.R. Spangler, *ApJ* **670**, 841 (2007).

[14] S. Srikanth, J. Ruff, and A.J. Fenn, *EVLA Memo* **95**, (2005).

[15] C.T. Stelzried et al., *SoPh* **14**, 2, 440 (1970).

[16] H. Zirin, B.M. Baumert and G.J. Hurford, *ApJ* **668**, 520 (1991).